



# Promoted electro-oxidation kinetics in chromium-doped $\alpha$ -Ni(OH)<sub>2</sub> nanosheets for efficient selective conversion of methanol to formate

Yu Fan, Xu Yang, Enhui Wei, Yuan Dong, Hongtao Gao, Xiliang Luo, Wenlong Yang\*

Key Laboratory of Optic-electric Sensing and Analytical Chemistry for Life Science, MOE, Key Laboratory of Analytical Chemistry for Life Science in Universities of Shandong, College of Chemistry and Molecular Engineering, Qingdao University of Science and Technology, Qingdao 266042, PR China

## ARTICLE INFO

### Keywords:

Ultrathin nanosheets  
Elemental doping  
Nickel hydroxide  
Electro-oxidation  
Methanol upgrading

## ABSTRACT

Owing to the elusive pathways of methanol oxidation reaction (MOR) and the lack of applicable catalysts, the selective electro-oxidation of methanol to formate remains a challenging topic. Herein, we present a chromium-doping strategy to promote the MOR performance of  $\alpha$ -Ni(OH)<sub>2</sub> nanosheets with a high selectivity towards formate generation. Taking chromium-doped  $\alpha$ -Ni(OH)<sub>2</sub> nanosheets as an example, we further highlight the role of doping atoms in MOR by combining theoretical calculations with experimental measurements. It reveals that chromium doping can not only enhance the conductivity of  $\alpha$ -Ni(OH)<sub>2</sub> nanosheets, but also endow the catalyst with optimized kinetics for electroactive NiOOH formation and methanol absorption, thus resulting in a remarkable MOR current density of 141 mA cm<sup>-2</sup> at 0.50 V vs. Ag/AgCl with a faradaic efficiency of 92.1% for formate. Furthermore, in situ infrared spectroscopy demonstrates that methanol is selectively oxidized to formate without further oxidation to CO<sub>2</sub> over chromium-doped  $\alpha$ -Ni(OH)<sub>2</sub> nanosheets in alkaline media.

## 1. Introduction

As an indispensable intermediate widely applied in textile, printing and pharmacy in chemical industry, formate holds an increasing market demand with the size predicted to reach 1 million tons by 2030 [1–3]. Traditional industrial strategies to produce formate compounds usually utilize the hydrolysis of methyl formate prepared from methanol reacting with CO under high temperature and high pressure, which involves the high energy consumption and hazardous gas management, thus inevitably raising the price of formate [4,5]. In this regard, electrocatalytic biomass valorization, especially methanol oxidation reaction (MOR) shows great promise in the field of chemical synthesis due to its appealing advantages of cost effectiveness and energy conservation, which can potentially achieve sustainable conversion of cheap methanol to value-added formate without CO<sub>2</sub> emissions. Moreover, as a promising alternative to the anodic oxygen evolution reaction (OER), the MOR can be further coupled with hydrogen evolution at the cathode to accomplish green energy production concurrently [6–8]. Nevertheless, the MOR constitutionally suffers from sluggish kinetics primarily related to its complex multi-electron transfer process and needs the utilization of advanced electrocatalysts to promote the overall catalytic efficiency [9,10]. By far, precious-metal catalysts have been known to be most

active in boosting the electrocatalytic MOR process, but their high cost and inferior tolerance to CO poisoning severely hinder the practical applications [11,12]. Therefore, it is of essential significance to design and develop cost-effective alternatives as highly efficient and durable electrocatalysts for selectively converting methanol to formate production.

Recently, nickel-based catalysts have attracted considerable attention in electrocatalysis because of their low cost and versatile electrochemical properties [13–15]. However, the MOR performance of nickel-based electrocatalysts remains largely below what is expected and their reaction mechanisms are still uncertain owing to the elusive MOR pathways. To this end, some effectual amelioration strategies including heterointerface engineering, doping regulation and defect engineering have been deliberately implemented to increase the electrical conductivity and number of active sites of nickel-based catalysts, so as to significantly enhance their final electrocatalytic performance [16–19]. Particularly, elemental doping shows potency in modifying electronic structures of materials, providing an effective solution to optimize their physicochemical characteristics and electrochemical behaviors for tunable catalytic activities [20–23]. Nevertheless, the inhomogeneous doping or excessive dopants may trigger the aggregation of dopants and even the formation of a secondary phase, possibly resulting

\* Corresponding author.

E-mail address: [wlyang@qust.edu.cn](mailto:wlyang@qust.edu.cn) (W. Yang).

<https://doi.org/10.1016/j.apcatb.2024.123716>

Received 9 November 2023; Received in revised form 23 December 2023; Accepted 6 January 2024

Available online 9 January 2024

0926-3373/© 2024 Elsevier B.V. All rights reserved.

in an adverse influence on both structural and electronic properties. Most notably, the incorporation of aliovalent dopants into the matrix of parent materials is usually accompanied by the introduction of extrinsic defects or structural distortions, which inevitably exerts a profound influence on their electronic structures and consequential electrocatalytic activities, rendering it difficult to gain fundamental insights into the authentic role of heteroatoms in electrocatalysis [24,25]. Note that ultrathin  $\alpha$ -Ni(OH)<sub>2</sub> nanosheets with atomic-level thickness have exhibited great superiority in optimizing electrochemical properties for small molecule oxidation owing to their highly exposed electroactive surface and adjustable electronic structures [26,27]. Especially, their ultrathin two-dimensional (2D) configuration with interlayer galleries allows a portion of nickel atoms to be substituted with other transition-metal elements, such as iron, cobalt, manganese, chromium, realizing homogeneous doping of heteroatoms throughout the catalyst to activate their inert basal planes, which will afford a desirable platform for establishing explicit structure-property relationships to exclusively elucidate how doping matters in electrocatalysis [28,29].

Herein, inspired by the above-mentioned considerations, ultrathin  $\alpha$ -Ni(OH)<sub>2</sub> nanosheets and its chromium-doped counterpart (Cr-doped Ni(OH)<sub>2</sub>) are first put forward as proof-of-concept catalytic models to shed light on the efficacy of doping atoms during the electrocatalytic MOR process. By combining the theoretical with experimental results, Cr doping endows  $\alpha$ -Ni(OH)<sub>2</sub> nanosheets with enhanced electrical conductivity, promoted formation of active NiOOH species and absorption ability of methanol, and thus favorable kinetics for the MOR. As expected, the Cr-doped  $\alpha$ -Ni(OH)<sub>2</sub> nanosheets exhibit excellent electrocatalytic MOR activity with a high faradaic efficiency for formate generation in alkaline solution. In situ infrared spectroscopy highlights the selective electro-oxidation of methanol to formate without the production of CO<sub>2</sub> or carbonates on the Cr-doped  $\alpha$ -Ni(OH)<sub>2</sub> nanosheets electrode. This work may bring some new opportunities for biomass valorization in the field of chemical industry.

## 2. Experimental section

### 2.1. Materials

All reagents were of analytical reagent grade, purchased from Sino-pharm Chemical Reagent Co., Ltd., and used as received without further purification.

### 2.2. Synthesis of Cr-doped $\alpha$ -Ni(OH)<sub>2</sub> nanosheets and pristine $\alpha$ -Ni(OH)<sub>2</sub> nanosheets

Typically, 0.9 mmol NiCl<sub>2</sub>·6 H<sub>2</sub>O, 0.1 mmol CrCl<sub>3</sub>·9 H<sub>2</sub>O and 0.5 mmol ammonium persulfate were in turn dissolved in 100 mL water with vigorous stirring for 5 min to achieve a transparent solution. Then, the precipitation was immediately formed when 1 mL of 28% ammonia solution was added into the above solution drop by drop under vigorous stirring. After that, the precipitation was collected by centrifugation and washed with distilled water and ethanol for several times, then dried in air at 60 °C for further characterization. The synthesis for pristine Ni(OH)<sub>2</sub> nanosheets was similar to that for ultrathin Cr-doped Ni(OH)<sub>2</sub> nanosheets except that the initial reactant was 1 mmol NiCl<sub>2</sub>·6 H<sub>2</sub>O without the addition of CrCl<sub>3</sub>·9 H<sub>2</sub>O.

### 2.3. Characterization

X-ray diffraction patterns (XRD) were acquired on Japan Rigaku D/max-rA equipped with graphite monochromatized high-intensity Cu K $\alpha$  radiation ( $\lambda$  = 1.54178 Å). The transmission electron microscopy (TEM) and high-resolution transmission electron microscopy (HRTEM) images were obtained on a JEOL-2010 TEM at an acceleration voltage of 200 kV. The high-angle annular dark-field scanning transmission electron microscopy (HAADF-STEM) and corresponding energy-dispersive

spectroscopy (EDX) mapping analyses were carried out on a JEOL JEM-ARF200F TEM/STEM. Atomic force microscopy (AFM) was performed by applying a DI Innova Multimode SPM platform. X-ray photoelectron spectroscopy (XPS) was measured on an ESCALAB MKII X-ray photoelectron spectrometer with an excitation source of Mg K $\alpha$  = 1253.6 eV. Raman spectra were achieved on a confocal micro-Raman spectrometer Lab-RAMARAMIS Horiba Jobin-Yvon apparatus with a laser excitation wavelength of 532 nm with appropriate filters. Ultraviolet photoemission spectroscopy (UPS) was recorded on a Thermo Scientific Escalab 250Xi spectrometer by using a monochromatic He I light source (21.22 eV). The CH<sub>3</sub>OH temperature programmed desorption-mass spectrometry (CH<sub>3</sub>OH-TPD-MS) analyses were performed on a Micromeritics ASAP 2920 system equipped with an HPR-20 R&D mass detector, the electric current and voltage of the mass detector under working condition was 20  $\mu$ A and 800 V, respectively. Individual  $m/z$  profiles were recorded over the mass range of 1–300 amu, and purified He was employed as the carrier gas. Nuclear magnetic resonance (NMR) spectra (1 H NMR) were obtained using a Bruker AV500 spectrometer.

In situ Fourier transformed infrared (FTIR) spectra were collected on a Thermo Scientific Nicolet 6700 FT-IR spectrometer equipped with attenuated total reflection (ATR) configuration using a liquid nitrogen cooled MCT-A detector. Briefly, 5 mg of catalysts and 40  $\mu$ L of 5 wt% Nafion solution were dispersed in 300  $\mu$ L of water and 660  $\mu$ L of ethanol solution to form a homogeneous ink by vigorous sonication. Then, 20  $\mu$ L of the above catalyst ink was dropped on a smooth glassy carbon electrode with a diameter of 6 mm as the working electrode (WE) that was pressed against a CaF<sub>2</sub> crystal (2 mm in thickness) in Infrared Reflection Absorption Spectroscopy (IRAS) test. As for the attenuated total reflection infrared absorption spectroscopy (ATR-IR) test, 40  $\mu$ L of the above catalyst ink was loaded on a thin Au film deposited onto on the reflection plane of a Si prism as the WE. In both measurements, the resolution of spectra was set to 4.0 cm<sup>-1</sup> with 32 scans per spectrum and the angle of incident beam was set to be 60°. The electrolyte was 1.0 M KOH containing 0.5 M methanol. A saturated Ag/AgCl electrode and a graphite electrode were applied as the reference electrode (RE) and the counter electrode (CE), respectively. The chronopotentiometry was recorded after 60 s electrolysis at different potentials ranging from 0 to 0.80 V vs. Ag/AgCl in 1.0 M KOH containing 0.5 M methanol.

### 2.4. Electrochemical measurements

All electrochemical measurements were carried out in a three-electrode system on an electrochemical station (CHI660B) by applying a saturated Ag/AgCl electrode as the reference electrode, a graphite electrode as the counter electrode and a glassy carbon electrode with catalysts as the working electrode. In a typical procedure, 4 mg of catalysts and 30  $\mu$ L of Nafion solutions (5 wt%, Sigma-Aldrich) were well dispersed by sonication to form a homogeneous ink in 1 mL of water-isopropanol solution (volume ratio of 3:1). Then, 5  $\mu$ L of the above catalyst dispersion was well dropped onto a glassy carbon electrode (GCE, 3 mm in diameter). Thus, the catalyst mass loading was estimated to be about 0.277 mg cm<sup>-2</sup> on the GCE. Cyclic voltammetry (CV) was performed in 1.0 M KOH solution with and without 0.5 M methanol at a scan rate of 50 mV s<sup>-1</sup>. Electrochemical impedance spectroscopy (EIS) was collected at different potentials in 1.0 M KOH solution containing 0.5 M methanol. The amplitude of the applied voltage was 5 mV, and the frequency range was 100 K Hz to 1 Hz. Chronoamperometry was performed in 1.0 M KOH solution containing 0.5 M methanol at a potential of 0.40 V vs. Ag/AgCl. The double layer capacitance ( $C_{dl}$ ) was derived from the CV curves in a non-faradaic potential region of 0.16 to 0.20 V vs. Ag/AgCl at different scan rates from 1 to 10 mV s<sup>-1</sup>. The  $C_{dl}$  value was determined by the linear plots of current density difference at 0.18 V vs. Ag/AgCl against the scan rate, which is half of the corresponding linear slope.

### 3. Results and discussion

#### 3.1. Theoretical calculations for the effect of Cr doping on the MOR activity

Density functional theory (DFT) calculations were applied for disclosing the atomic-level regulation of chromium doping on the electronic structure of  $\alpha$ -Ni(OH)<sub>2</sub> nanosheets (Fig. S1). As shown in Fig. 1a, the calculated density of states (DOS) of the Cr-doped Ni(OH)<sub>2</sub> system exhibit an obviously reduced bandgap of about 1.19 eV with respect to the pristine Ni(OH)<sub>2</sub> system (2.65 eV), indicating the improved conductive property upon the replacement of nickel with chromium atoms in Ni(OH)<sub>2</sub> layers. Also, the substitutional doping of Cr ions brings some new energy levels between the valence and conduction bands in Cr-doped Ni(OH)<sub>2</sub> system, which can be probably associated with the splitting of Cr 3d orbitals [30,31]. In this circumstance, the excitation of electrons can more readily occur benefitting from the d-d electronic transitions of Cr ions in octahedral coordination, enabling a great opportunity to achieve enhanced charge transfer ability and higher electrocatalytic MOR efficiency. Importantly, the d-band center, which serves as an essential electronic descriptor for predicting the catalytic reactivity of 3d transition-metal catalysts, can be precisely tailored by transition-metal doping [32,33]. The d band centers relative to the Fermi level ( $E_F$ , 0 eV in Figs. 1a and 1b) are respectively calculated to be  $-5.50$  and  $-3.99$  eV for Cr-doped Ni(OH)<sub>2</sub> and pristine Ni(OH)<sub>2</sub>, revealing the obvious downshift of d band center position after the incorporation of Cr ions into Ni(OH)<sub>2</sub> structure. This is significantly conducive to facilitating the desorption of hydrogen atoms from lattice hydroxyl group of  $\alpha$ -Ni(OH)<sub>2</sub> to generate more electroactive NiOOH species towards methanol oxidation. To further verify this, the energy needed for the dehydrogenation reaction ( $\text{Ni(OH)}_2 + \text{OH}^- = \text{NiOOH} +$

$\text{H}_2\text{O} + \text{e}^-$ ) was further evaluated and displayed in Fig. 1c, S2 and Table S1. Evidently, the calculated NiOOH formation energy for Cr-doped Ni(OH)<sub>2</sub> system (0.89 eV) is much lower than that for pristine Ni(OH)<sub>2</sub> system (1.64 eV), indicating that Cr doping endows the  $\alpha$ -Ni(OH)<sub>2</sub> catalyst with accelerated generation of electroactive NiOOH species that is strongly related to the electro-oxidation ability of nickel-based catalysts. Moreover, from the viewpoint of kinetic modulation, the adsorption behavior of methanol molecule onto the catalytic sites plays a non-ignorable role in optimizing the electrocatalytic MOR process [8,34]. As elaborated in Fig. 1d, S3 and Table S2, the methanol adsorption energy for Cr-doped Ni(OH)<sub>2</sub> system is calculated to be  $-0.64$  eV, smaller than that for pristine Ni(OH)<sub>2</sub> system ( $-0.45$  eV), which signifies that the Cr-doped Ni(OH)<sub>2</sub> surface is thermodynamically more favorable for the adsorption of methanol molecule, leading to an increased local methanol concentration and thus drastically enhancing the MOR performance. Accordingly, the homogeneous doping of Cr atoms in  $\alpha$ -Ni(OH)<sub>2</sub> layers allows for higher electrical conductivity, easier electron excitation and promoted NiOOH formation kinetics and methanol adsorption, implying considerably improved electrocatalytic MOR performance.

#### 3.2. Catalyst characterization and discussion

As schematically illustrated in Fig. 2a, ultrathin  $\alpha$ -Ni(OH)<sub>2</sub> nanosheets and Cr-doped Ni(OH)<sub>2</sub> nanosheets were then synthesized through a simple liquid-phase reaction at room temperature. Inductively coupled plasma (ICP) analysis confirms the doping content of Cr is about 8.8%. The crystal structure of as-obtained samples was further investigated by powder X-ray diffraction (XRD) measurement. In Fig. 2b, all the diffraction peaks of Cr-doped Ni(OH)<sub>2</sub> nanosheets match well with those of the  $\alpha$ -Ni(OH)<sub>2</sub> phase (JCPDS card No. 22-0444) without any

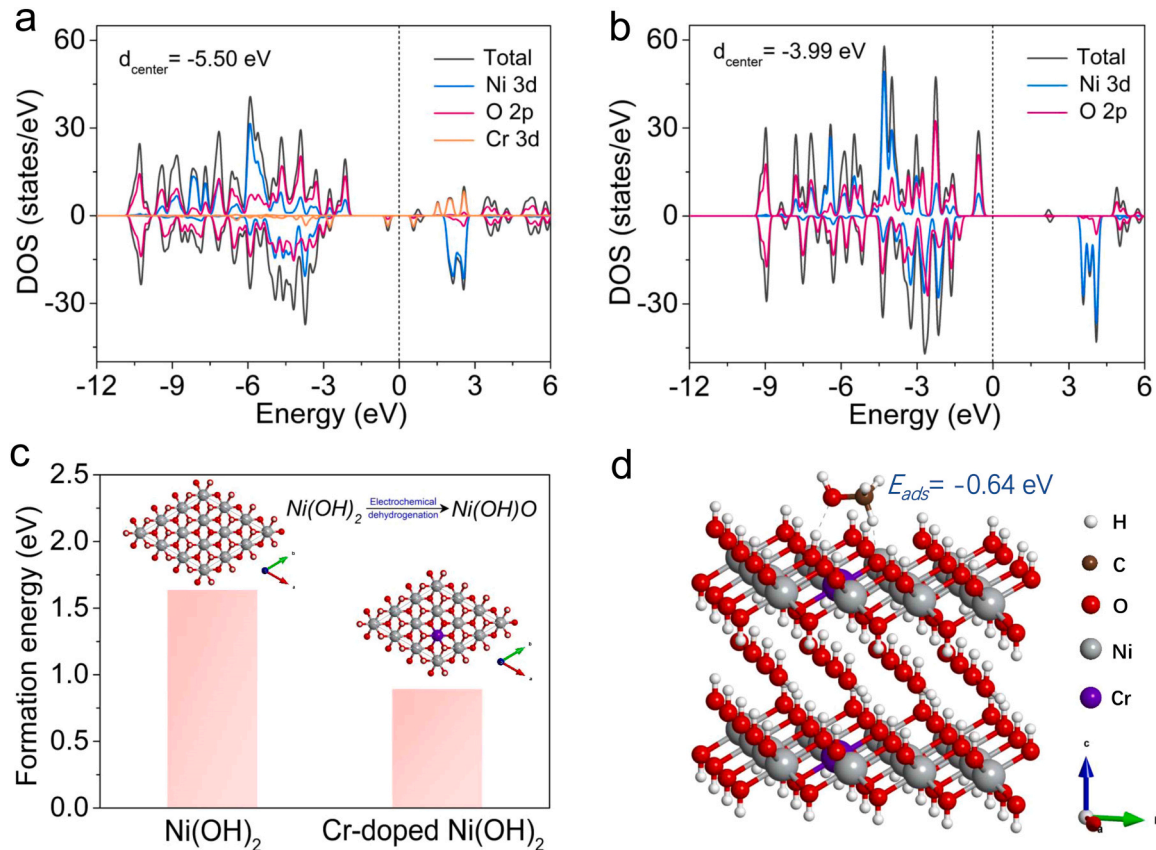


**Fig. 1.** The calculated density of states (DOS) of (a) Cr-doped Ni(OH)<sub>2</sub> slab and (b) pristine  $\alpha$ -Ni(OH)<sub>2</sub> slab. (c) The formation energies for Cr-doped Ni(OH)<sub>2</sub> and pristine  $\alpha$ -Ni(OH)<sub>2</sub> based on the electrochemical dehydrogenation reaction. (d) The adsorption energy of methanol onto the Cr-doped Ni(OH)<sub>2</sub> surface.



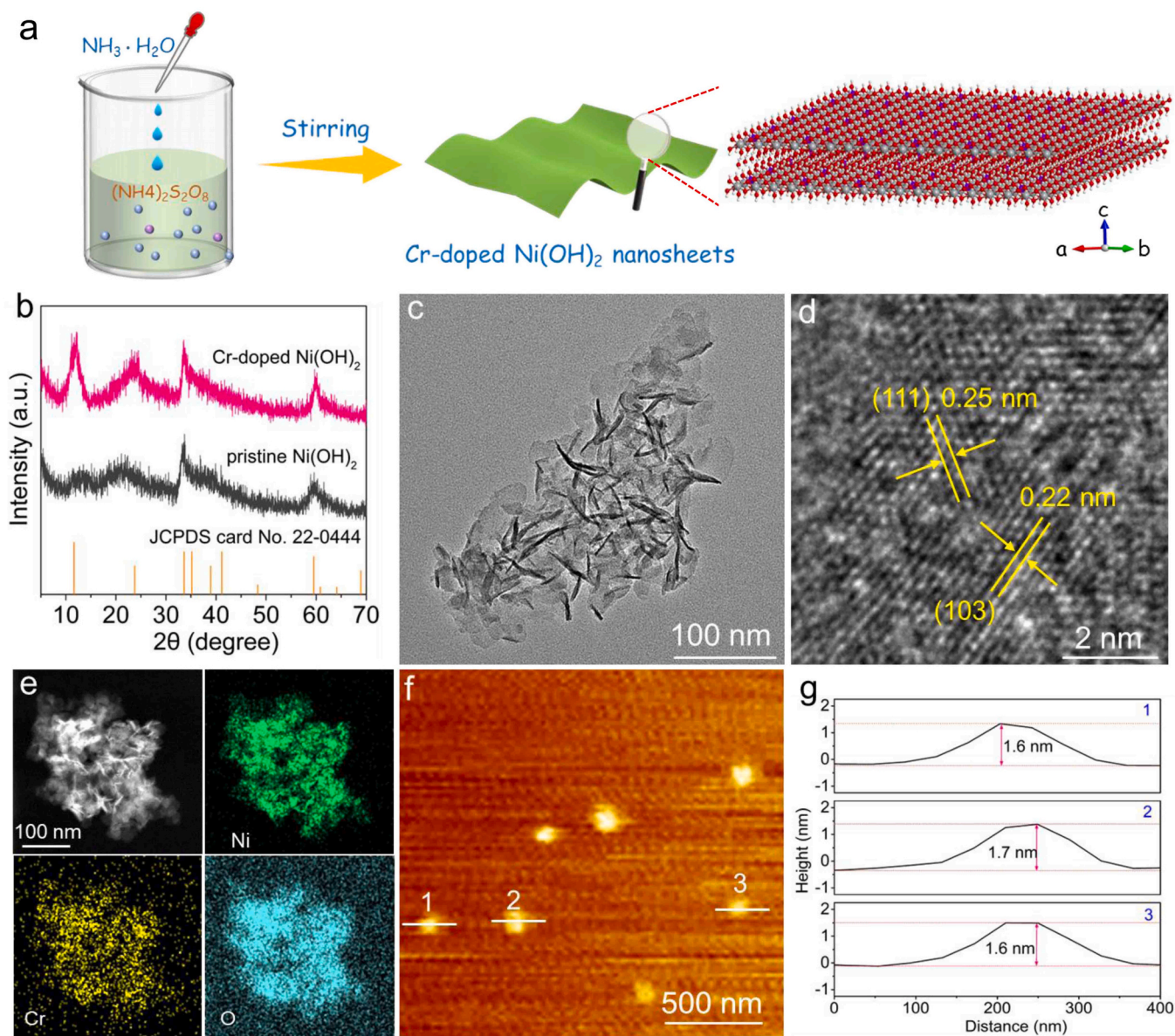


**Fig. 2.** (a) Schematic illustration for the synthesis of ultrathin Cr-doped  $\text{Ni}(\text{OH})_2$  nanosheets. (b) XRD patterns of ultrathin Cr-doped  $\text{Ni}(\text{OH})_2$  nanosheets and pristine  $\text{Ni}(\text{OH})_2$  nanosheets. (c) TEM image, (d) HRTEM image, (e) HAADF-STEM image and corresponding EDX elemental mapping images, (f) AFM image and (g) corresponding height profiles of ultrathin Cr-doped  $\text{Ni}(\text{OH})_2$  nanosheets.

impurity, manifesting that Cr doping does not alter the pristine crystal structure of  $\alpha\text{-Ni}(\text{OH})_2$ . Furthermore, the sheet-like morphology of Cr-doped  $\text{Ni}(\text{OH})_2$  and pristine  $\alpha\text{-Ni}(\text{OH})_2$  samples can be observed from the transmission electron microscopy (TEM) images (Fig. 2c and S4), and the nearly transparent feature suggests their ultrathin thickness. Atomic force microscopy (AFM) image in Fig. 2f and corresponding height profiles in Fig. 2g reveal the average thickness of Cr-doped  $\text{Ni}(\text{OH})_2$  nanosheets to be approximately 1.6 nm, which is consistent with two  $\alpha\text{-Ni}(\text{OH})_2$  layers along the c-axis. Moreover, the high-resolution TEM (HRTEM) image in Fig. 2d shows intact lattice fringes with interplanar distances of 0.25 and 0.22 nm corresponding to the (111) and (103) planes of  $\alpha\text{-Ni}(\text{OH})_2$ , illustrating the absence of detectable structural distortions or defects after Cr doping. Additionally, Fig. 2e displays the high-angle annular dark-field scanning TEM (HAADF-STEM) image and the corresponding energy-dispersive X-ray spectroscopic (EDX) element mapping of Cr-doped  $\text{Ni}(\text{OH})_2$  nanosheets, visually depicting the uniform distribution of Ni, Cr and O elements in the doped ultrathin nanosheets.

X-ray photoelectron spectroscopy (XPS) was further carried out to investigate the chemical composition and valence states of the Cr-doped  $\text{Ni}(\text{OH})_2$  nanosheets. As shown in Fig. S5, the XPS survey spectra also confirms the coexistence of Ni, Cr and O elements. The high-resolution Ni 2p spectra in Fig. 3a presents two noticeable peaks at 855.7 and 873.3 eV indexed to the Ni 2p<sub>3/2</sub> and Ni 2p<sub>1/2</sub> with a spin-energy separation of 17.6 eV, together with two shakeup satellites, matching well with the characteristic of  $\text{Ni}(\text{OH})_2$  phase [35]. Apparently, the Cr 2p<sub>3/2</sub> and Cr 2p<sub>1/2</sub> peaks in the high-resolution Cr 2p spectra (Fig. 3b) can be deconvoluted into two distinct spin-orbit doublets. In particular, the prominent fitted peaks at 579.0 and 588.3 eV are ascribable to signals of  $\text{Cr}^{6+}$ , while the other weaker peaks at 576.4 and 586.6 eV are associated to the presence of  $\text{Cr}^{3+}$ , which manifests that the majority of Cr dopants are in + 6 oxidation states [36,37]. Raman spectroscopy (Fig. 3c) was applied to analyze the structural information of Cr-doped  $\text{Ni}(\text{OH})_2$  nanosheets. Notably, the broad peak at 536  $\text{cm}^{-1}$  is assignable to the Ni-O stretching mode of  $\alpha\text{-Ni}(\text{OH})_2$  phase [38]. Whereas the weak peak at 364  $\text{cm}^{-1}$  belongs to the bending vibration of  $\text{Cr}^{3+}\text{-O}$ , and the strong

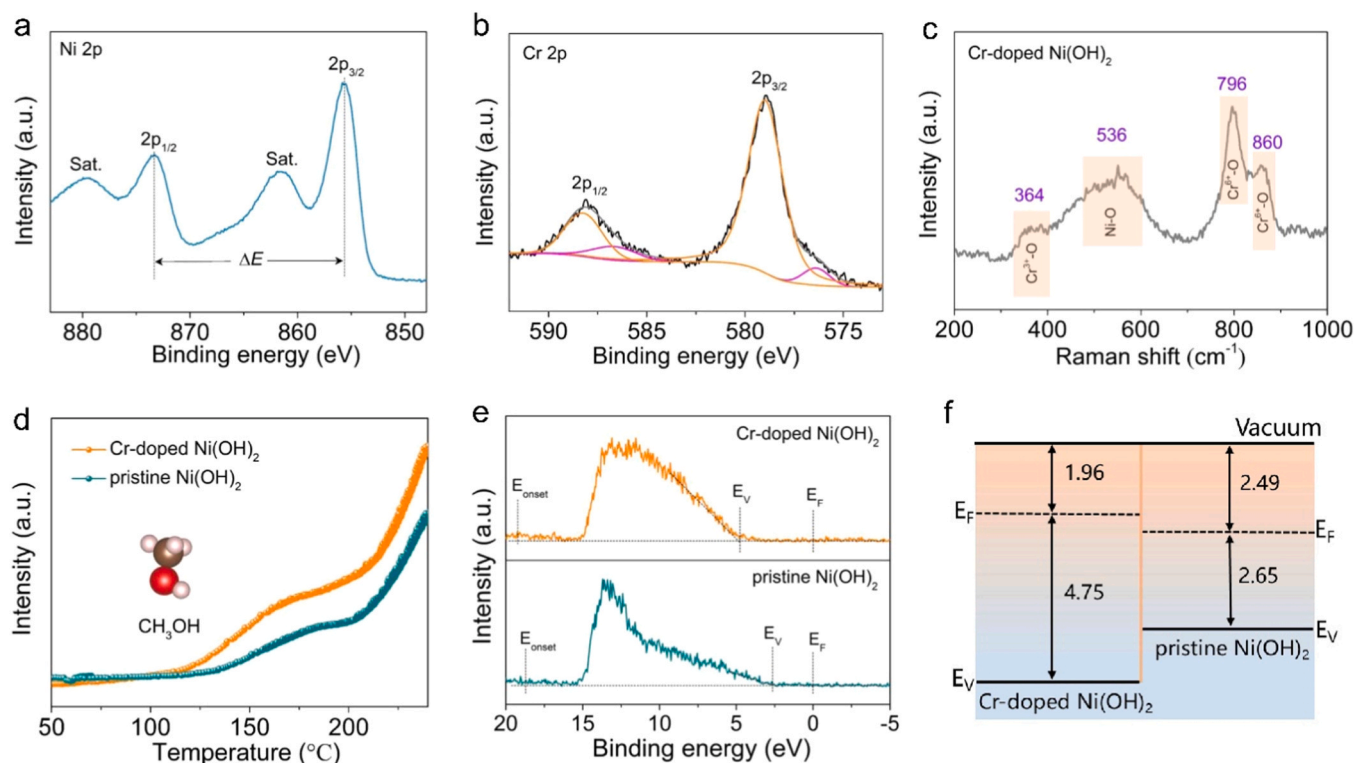


**Fig. 3.** (a) Ni 2p spectra, (b) Cr 2p spectra and (c) Raman spectra of Cr-doped Ni(OH)<sub>2</sub> nanosheets. (d) TPD-MS curves of Cr-doped Ni(OH)<sub>2</sub> and pristine Ni(OH)<sub>2</sub> nanosheets for methanol. (e) UPS spectra, (f) Schematic energy band diagrams of Cr-doped Ni(OH)<sub>2</sub> and pristine Ni(OH)<sub>2</sub> nanosheets deduced by the UPS data.

peaks at 796 and 860 cm<sup>-1</sup> correspond to the stretching vibration of Cr<sup>6+</sup>-O, unveiling the coexistence of Cr<sup>3+</sup> and Cr<sup>6+</sup> ions [39,40], in good agreement with the XPS results. As noted above, the adsorption behavior of methanol molecules onto the catalyst surface is crucial for the MOR, which was studied by the temperature programmed desorption-mass spectrometry (TPD-MS). In Fig. 3d, the broad peak in the region of 120–200 °C for both samples can be attributed to the desorption of methanol molecules. By contrast, the methanol desorption peak for Cr-doped Ni(OH)<sub>2</sub> nanosheets are evidently larger than that for pristine Ni(OH)<sub>2</sub> nanosheets, demonstrating its stronger methanol adsorption and storage capacity, which is consistent well with the DFT results. Moreover, ultraviolet photoelectron spectroscopy (UPS) was employed to investigate the impacts of Cr doping on the electronic properties of α-Ni(OH)<sub>2</sub> nanosheets. As shown in Fig. 3e, the work function (E<sub>Φ</sub>) values for pristine Ni(OH)<sub>2</sub> and Cr-doped Ni(OH)<sub>2</sub> nanosheets are respectively calculated to be 2.49 and 1.96 eV by means of the equation  $E_{\Phi} = h\nu - E_{\text{onset}}$ , where  $h\nu$  represents the incident photon energy (21.22 eV) and  $E_{\text{onset}}$  is the onset level related to the secondary edge. Furthermore, the valence band maximum (E<sub>V</sub>) can be determined by linearly extrapolating the leading edge of the UPS spectrum to the baseline, which are positioned 2.65 and 4.75 eV below the E<sub>F</sub> of pristine Ni(OH)<sub>2</sub> and Cr-doped Ni(OH)<sub>2</sub> nanosheets, respectively. As illustrated in Fig. 3f, the schematic energy band alignment diagrams were achieved in terms of the UPS results. By comparison, a lower E<sub>Φ</sub> value and higher E<sub>F</sub> level for Cr-doped Ni(OH)<sub>2</sub> nanosheets indicate its better electrical conductivity with respect to pristine Ni(OH)<sub>2</sub> nanosheets [41,42]. Besides, the E<sub>V</sub> for Cr-doped Ni(OH)<sub>2</sub> nanosheets is much further away from the E<sub>F</sub> level, suggesting the d band center of α-Ni(OH)<sub>2</sub> nanosheets is downshifted from the E<sub>F</sub> level upon Cr doping since d states are mainly attributed to the valence electrons near the E<sub>F</sub> level [32].

### 3.3. Evaluation of electrocatalytic performance for MOR

To clarify the efficacy of Cr doping on the electro-oxidation

performance, the electrocatalytic OER and MOR activity of each electrode was evaluated in 1.0 M KOH electrolyte in the absence and presence of 0.5 M methanol. As displayed by CV curves in Fig. 4a, the anodic current density for Cr-doped Ni(OH)<sub>2</sub> electrode increases sharply once 0.5 M methanol was introduced to the electrolyte at a sweep rate of 50 mV s<sup>-1</sup>, indicating the excellent electrocatalytic response for methanol oxidation. Also, the nearly overlapped anodic MOR curves in the forward and backward scanning manifests few toxic intermediates involved in the electrocatalytic pathway [43]. By contrast, only a mildly enhanced anodic current density is achieved on the pristine Ni(OH)<sub>2</sub> electrode after adding methanol, revealing its comparatively inferior MOR activity at the same potential (Fig. S6). Notably, a small potential of 0.422 V vs. Ag/AgCl on the Cr-doped Ni(OH)<sub>2</sub> electrode is demanded to deliver a current density of 50 mA cm<sup>-2</sup> for the MOR, with a negative shift of 246 mV as compared to that for the OER, corroborating the accelerated anode kinetics when catalyzing methanol oxidation. Such a prominent difference between two reaction kinetics is further demonstrated by their corresponding Tafel plots in Fig. S7, which is conducive to the oxidation of methanol before the OER becomes prevalent. Fig. 4b contrasts the CV curves of the two electrodes for the MOR. It is obvious that the Cr-doped Ni(OH)<sub>2</sub> electrode possesses a superior electrocatalytic MOR activity with respect to pristine Ni(OH)<sub>2</sub> electrode, reflected from its lower onset potential and higher anodic current density in the region of methanol oxidation. In particular, the onset potential of Cr-doped electrode is found to be 0.378 V vs. Ag/AgCl, showing an obvious negative shift of 81 mV compared to that of pristine Ni(OH)<sub>2</sub> electrode. Impressively, the MOR current density of Cr-doped Ni(OH)<sub>2</sub> electrode reaches 141 mA cm<sup>-2</sup> at a potential of 0.50 V vs. Ag/AgCl, which is about 11.6 times larger than of pristine Ni(OH)<sub>2</sub> electrode and even comparable to other highly efficient Ni-based electrocatalysts reported (Table S3). Fig. 4c displays that the Tafel slope of 27.5 mV dec<sup>-1</sup> for Cr-doped Ni(OH)<sub>2</sub> electrode is much lower than that for pristine Ni(OH)<sub>2</sub> electrode (128.6 mV dec<sup>-1</sup>), highlighting the dramatically promoted MOR kinetics primarily derived from Cr doping. Furthermore,



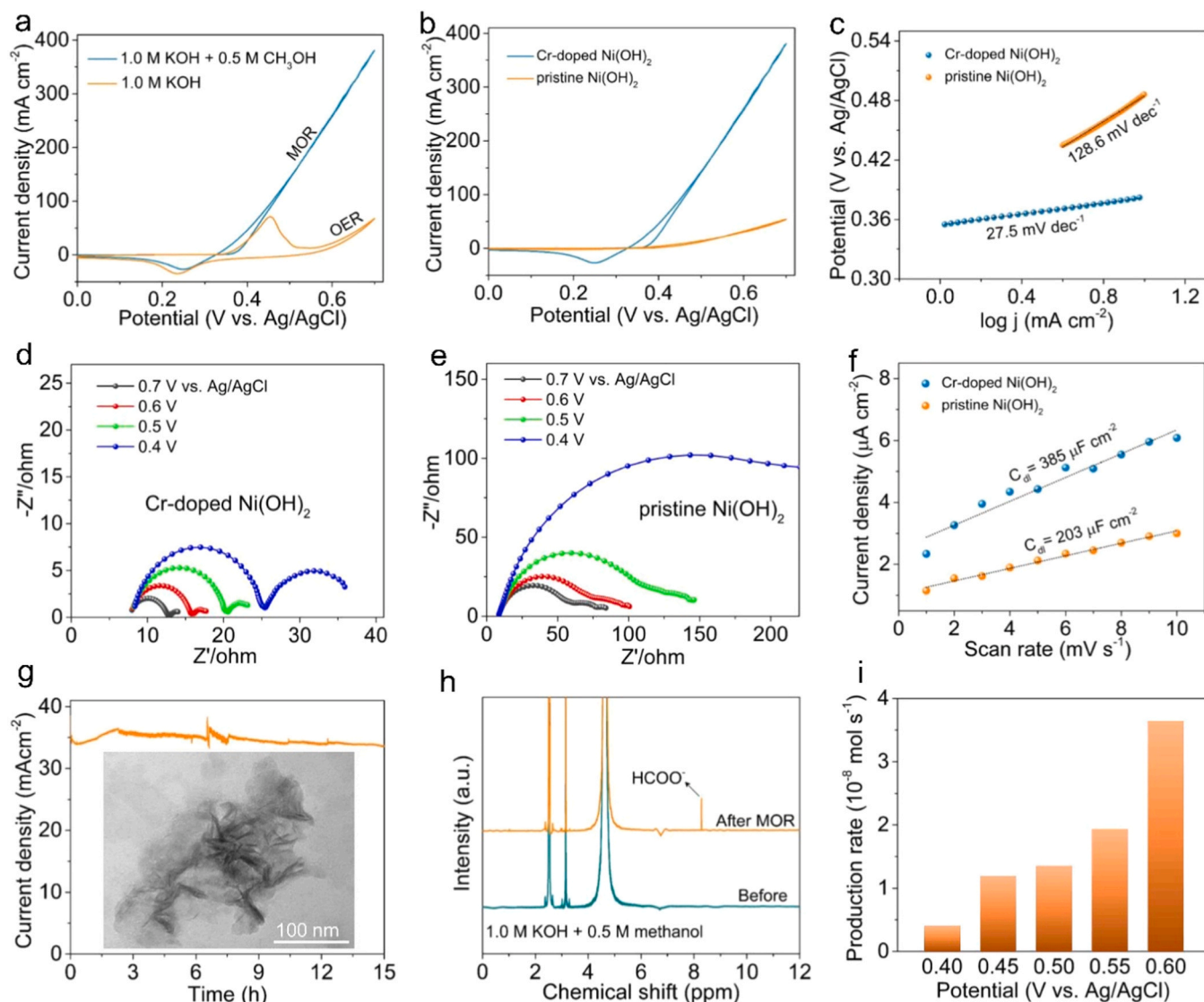


**Fig. 4.** (a) Cyclic voltammetry (CV) curves of Cr-doped  $\text{Ni}(\text{OH})_2$  nanosheets recorded in 1.0 M KOH with and without 0.5 M methanol at a scan rate of  $50 \text{ mV s}^{-1}$ . (b) CV curves, (c) corresponding Tafel plots of Cr-doped  $\text{Ni}(\text{OH})_2$  and pristine  $\text{Ni}(\text{OH})_2$  nanosheets in 1.0 M KOH with 0.5 M methanol. (d, e) Nyquist plots measured at varied potentials in 1.0 M KOH with 0.5 M methanol. (f) Comparison of the  $C_{dl}$  values obtained in 1.0 M KOH solution. (g) Chronoamperometric curve and TEM image (inset) of Cr-doped  $\text{Ni}(\text{OH})_2$  nanosheets after stability test for the MOR. (h)  $^1\text{H}$  NMR spectra of the anode product after MOR operation in 1.0 M KOH with 0.5 M methanol. (i) The rates of formate generation at different potentials.

electrochemical impedance spectroscopy (EIS) was measured at different potentials to get insights into the interface behavior. As shown in Figs. 4d and 4e, Cr-doped  $\text{Ni}(\text{OH})_2$  electrode exhibits a smaller charge-transfer resistance ( $R_{ct}$ ) at relatively lower potentials compared with pristine  $\text{Ni}(\text{OH})_2$  electrode, verifying that Cr doping enables a faster interfacial electron transfer to boost the whole MOR process. Moreover, according to CV curves in a non-faradaic potential range (Fig. S8), the double-layer capacitance ( $C_{dl}$ ) was used to evaluate the electrochemically active surface area (ECSA) that has a great influence on the final performance of electrocatalysts. In Fig. 4f, the  $C_{dl}$  value for Cr-doped  $\text{Ni}(\text{OH})_2$  ( $385 \mu\text{F cm}^{-2}$ ) is determined to be about 1.9 times higher than that for pristine  $\text{Ni}(\text{OH})_2$  ( $203 \mu\text{F cm}^{-2}$ ), which is indicative of the more exposed electroactive sites on Cr-doped  $\text{Ni}(\text{OH})_2$  surface. Moreover, the CV curves for the MOR were further normalized by  $C_{dl}$  values to assess the intrinsic catalytic activity of every site. Obviously, Cr-doped  $\text{Ni}(\text{OH})_2$  nanosheets still possess a higher MOR current density at the same potential with respect to pristine sample (Fig. S9), unveiling its superior intrinsic reactivity towards the MOR. Also, Cr-doped  $\text{Ni}(\text{OH})_2$  nanosheets exhibit a satisfactory long-term electrochemical stability for

methanol oxidation. As revealed by chronoamperometric curve in Fig. 4g, the current density at a constant potential of 0.40 V vs. Ag/AgCl shows an ignorable diminishment even after 15 h continuous operation in 1.0 M KOH with 0.5 M methanol. The TEM image (inset) consistently discloses that the initial morphology of Cr-doped  $\text{Ni}(\text{OH})_2$  nanosheets is substantially retained after the stability test, indicating its remarkable durability in a strong alkaline solution. Taken together, these results demonstrate the excellent electrocatalytic MOR activity and stability of Cr-doped  $\text{Ni}(\text{OH})_2$  nanosheets, emphasizing the regulatory effect of Cr doping on the electro-oxidation of methanol. In addition, the electrocatalytic oxidation products of methanol were analyzed by  $^1\text{H}$  nuclear magnetic resonance ( $^1\text{H}$  NMR). Fig. 4h reveals that formate is the only liquid product after the MOR in 1.0 M KOH with 0.5 M methanol, corroborating the selective electro-oxidation of methanol to formate over Cr-doped  $\text{Ni}(\text{OH})_2$  electrode [44]. Ion Chromatography (IC) analysis was further carried out at different voltages to quantify the produced formate after the MOR operation. Fig. 4i display that the average production rates of formate are evaluated to be about  $3.94 \times 10^{-9}$ ,  $1.18 \times 10^{-8}$ ,  $1.34 \times 10^{-8}$ ,  $1.93 \times 10^{-8}$  and  $3.63 \times 10^{-8} \text{ mol s}^{-1}$  at the

applied potential of 0.40, 0.45, 0.50, 0.55 and 0.60 V vs. Ag/AgCl, respectively. In addition, the faradaic efficiency for selective electrocatalytic conversion of methanol to formate is found to be 92.1% at a potential of 0.50 V vs. Ag/AgCl.

### 3.4. Mechanism investigations for the electrocatalytic MOR process

With a view to identifying the MOR activity origin, the electrochemical behavior of the electrocatalysts were further probed by cyclic voltammetry (CV) curves in 1.0 M KOH at different scan rates using a three-electrode system. As shown in Fig. S10, a pair of clear redox peaks can be ascribed to the reversible  $\text{Ni}^{2+}/\text{Ni}^{3+}$  transformation whose current densities are linearly proportional to the sweep rates ranging from 10 to  $150 \text{ mV s}^{-1}$ . Thus, the surface coverage ( $\Gamma^*$ ) of  $\text{Ni}^{2+}/\text{Ni}^{3+}$  redox species for each electrode was determined in light of the average slope of the anodic and cathodic data (Fig. 5a). Notably, the  $\Gamma^*$  value for the Cr-doped  $\text{Ni}(\text{OH})_2$  nanosheets is found to be  $6.07 \times 10^{-7} \text{ mol cm}^{-2}$ , approximately two times greater than that for pristine  $\text{Ni}(\text{OH})_2$  nanosheets (Fig. 5b), which is responsible for the larger MOR current density obtained on the Cr-doped  $\text{Ni}(\text{OH})_2$  electrode as the redox capacity of nickel-based electrode is associated with the formation of active  $\text{NiOOH}$  species. Besides, Fig. 5a presents the plots of peak current density against the square root of the scan rate, and their good linear dependences indicate the diffusion-dominated feature of the interconversion of  $\text{Ni}(\text{OH})_2/\text{NiOOH}$  [11]. As reported before, the proton diffusion coefficient ( $D$ ) is a key indicator for the description of oxidation behavior of electrocatalysts since the solid-phase body of proton

diffusion is deemed as the rate-limiting step for the electro-oxidation reaction [15]. According to the Randles-Sevcik equation, the  $D$  value (Fig. 5b) for Cr-doped  $\text{Ni}(\text{OH})_2$  electrode is determined to be  $6.11 \times 10^{-7} \text{ cm}^2 \text{ s}^{-1}$ , about 4.2-fold higher than that for pristine  $\text{Ni}(\text{OH})_2$  electrode ( $1.45 \times 10^{-7} \text{ cm}^2 \text{ s}^{-1}$ ), which allows a more negative onset oxidation potential on Cr-doped catalyst for the electrochemical MOR process. To deeply comprehend the methanol oxidation pathways over the Cr-doped  $\text{Ni}(\text{OH})_2$  electrode, in-situ infrared reflection absorption spectroscopy (IRAS) and attenuated total reflection infrared absorption spectroscopy (ATR-IR) were performed in a 1.0 M KOH electrolyte with 0.5 M methanol to monitor the evolution of relevant intermediates and products during the MOR process. As shown in Fig. 5c, several IR absorption bands at around 1583, 1383 and  $1352 \text{ cm}^{-1}$  in the IRAS spectrum are readily ascribed to the presence of  $\text{HCOO}^-$  ions, while the adsorption peaks appeared in the range  $1000\text{--}1200 \text{ cm}^{-1}$  can be associated with the consumption of methanol molecules [8,45]. Apparently, negligible peaks related to  $\text{HCOO}^-$  can be observed when the applied voltage below 0.40 V vs. Ag/AgCl, which suggests that methanol oxidation does not occur at these potentials. As the voltage progressively increases, the intensity of above  $\text{HCOO}^-$  peaks enhances sharply, demonstrating the electro-oxidation of methanol to formate in the electrolyte. As for the ATR-IR spectrum in Fig. 5d, a broad peak at  $1325 \text{ cm}^{-1}$  can be ascribed to the generation of adsorbed  $\text{HCOO}^*$  intermediates [46], along with the absorption bands at about 1585, 1383 and  $1345 \text{ cm}^{-1}$  associated to formate, directly confirming the selective conversion of methanol-to-formate pathway on the catalyst surface. Of note, no observable signal assigned to CO species or  $\text{CO}_2$

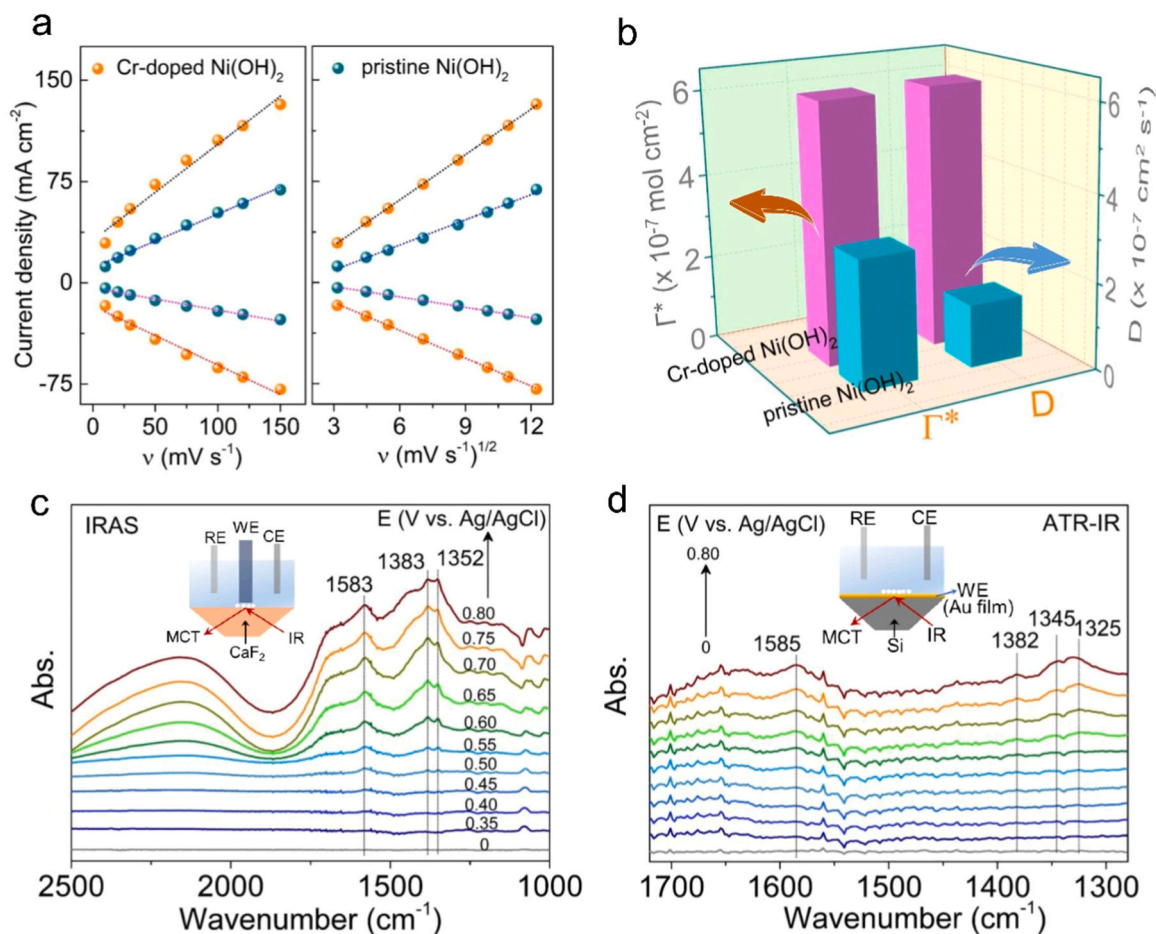


**Fig. 5.** (a) The linear dependence between the anodic and cathodic current densities and the scan rates (left), and the square root of the scan rates (right) in 1.0 M KOH electrolyte. (b) The estimated  $\Gamma^*$  values and  $D$  values for Cr-doped  $\text{Ni}(\text{OH})_2$  and pristine  $\text{Ni}(\text{OH})_2$  nanosheets. (c) In situ IRAS spectrum and (d) ATR-IR spectrum of the MOR on the Cr-doped  $\text{Ni}(\text{OH})_2$  nanosheets surface at different potentials in 1.0 M KOH electrolyte containing 0.5 M methanol.

production can be detected from the IRAS and ATR-IR spectrum even when the anodic potential exceeds 0.80 V vs. Ag/AgCl, undoubtedly excluding the toxic CO-pathway during the MOR process [44,45]. Based on the above results, the possible MOR mechanism on the Cr-doped Ni(OH)<sub>2</sub> electrode in alkaline media may be proposed briefly as follows: (1) the initial formation of active NiOOH species, (2) the adsorption of CH<sub>3</sub>OH molecules onto active sites, (3) the selective oxidation of CH<sub>3</sub>OH to formate.

#### 4. Conclusions

In summary, a simple and effectual Cr-doping strategy was adopted to enhance the electrocatalytic MOR activity of  $\alpha$ -Ni(OH)<sub>2</sub> nanosheets for highly selective conversion of methanol into formate. Theoretical and experimental investigations were implemented to comprehensively clarify the role that Cr atoms play in MOR. The ultrathin Cr-doped  $\alpha$ -Ni(OH)<sub>2</sub> nanosheets exhibited increased electrical conductivity and promoted generation of active species and absorption of methanol, enabling a more favorable catalytic kinetics for the MOR, which showed 11.6-fold larger MOR current density with respect to that of pristine  $\alpha$ -Ni(OH)<sub>2</sub> nanosheets and a high faradaic efficiency of 92.1% for formate generation at the potential of 0.50 V vs. Ag/AgCl. Moreover, in situ infrared spectroscopy was applied to get insights into the MOR mechanism, disclosing that Cr-doped  $\alpha$ -Ni(OH)<sub>2</sub> nanosheets could drive the selective electro-oxidation of methanol to formate without the production of CO<sub>2</sub> or carbonates in alkaline solution. This study highlights a promising plan for the design of highly active nickel-based electrocatalysts with remarkable MOR performance for methanol upgrading through elemental doping.

#### CRediT authorship contribution statement

**Yang Wenlong:** Data curation, Formal analysis, Investigation, Resources, Supervision, Validation, Writing – original draft, Writing – review & editing. **Wei Enhui:** Investigation. **Dong Yuan:** Investigation. **Gao Hongtao:** Software. **Luo Xiliang:** Resources, Supervision. **Yang Xu:** Investigation, Validation. **Fan Yu:** Data curation, Investigation, Validation, Writing – original draft.

#### Declaration of Competing Interest

The authors declare that they have no known competing financial interests or personal relationships that could have appeared to influence the work reported in this paper.

#### Data Availability

Data will be made available on request.

#### Acknowledgements

This work was supported by the National Natural Science Foundation of China (21805149, 21675093), the Natural Science Foundation of Shandong Province of China (ZR2018BB012, 2015ZRB01A0D), and the Taishan Scholar Program of Shandong Province of China (ts20110829).

#### Appendix A. Supporting information

Supplementary data associated with this article can be found in the online version at [doi:10.1016/j.apcatb.2024.123716](https://doi.org/10.1016/j.apcatb.2024.123716).

#### References

- [1] P. Zhu, H.T. Wang, High-purity and high-concentration liquid fuels through CO<sub>2</sub> electroreduction, *Nat. Catal.* 4 (2021) 943–951, <https://doi.org/10.1038/s41929-021-00694-y>.
- [2] B. Zhao, J.W. Liu, X.W. Wang, C.Y. Xu, P.F. Sui, R.F. Feng, L. Wang, J.J. Zhang, J. L. Luo, X.Z. Fu, CO<sub>2</sub>-emission-free electrocatalytic CH<sub>3</sub>OH selective upgrading with high productivity at large current densities for energy saved hydrogen co-generation, *Nano Energy* 80 (2021) 105530, <https://doi.org/10.1016/j.nanoen.2020.105530>.
- [3] X.Y. Guo, S.M. Xu, H. Zhou, Y. Ren, R.X. Ge, M. Xu, L.R. Zheng, X.G. Kong, M. F. Shao, Z.H. Li, H.H. Duan, Engineering hydrogen generation sites to promote electrocatalytic CO<sub>2</sub> reduction to formate, *ACS Catal.* 12 (2022) 10551–10559, <https://doi.org/10.1021/acscatal.2c02548>.
- [4] Q. Liu, L.P. Wu, S. Güllak, R. Nils, J. Ralf, B. Matthias, Towards a sustainable synthesis of formate salts: combined catalytic methanol dehydrogenation and bicarbonate hydrogenation, *Angew. Chem. Int. Ed.* 53 (2014) 7085–7088, <https://doi.org/10.1002/anie.201400456>.
- [5] J. Hao, J.W. Liu, D. Wu, M.X. Chen, Y. Liang, Q. Wang, L. Wang, X.Z. Fu, J.L. Luo, In situ facile fabrication of Ni(OH)<sub>2</sub> nanosheet arrays for electrocatalytic co-production of formate and hydrogen from methanol in alkaline solution, *Appl. Catal. B* 281 (2021) 119510, <https://doi.org/10.1016/j.apcatb.2020.119510>.
- [6] C.R. Liu, F.L. Yang, A. Schechter, L.G. Feng, Recent progress of Ni-based catalysts for methanol electrooxidation reaction in alkaline media, *Adv. Sens. Energy Mater.* 2 (2023) 100055, <https://doi.org/10.1016/j.asems.2023.100055>.
- [7] G.D. Fu, X.M. Kang, Y. Zhang, X.Q. Yang, L. Wang, X.Z. Fu, J.J. Zhang, J.L. Luo, J. W. Liu, Coordination effect-promoted durable Ni(OH)<sub>2</sub> for energy-saving hydrogen evolution from water/methanol CO-electrocatalysis, *Nano Micro Lett.* 14 (2022) 200, <https://doi.org/10.1007/s40820-022-00940-3>.
- [8] Y.X. Hao, D.S. Yu, S.Q. Zhu, C.H. Kuo, Y.M. Chang, L.Q. Wang, H.Y. Chen, M. H. Shao, S.J. Peng, Methanol upgrading coupled with hydrogen product at large current density promoted by strong interfacial interactions, *Energy Environ. Sci.* 16 (2023) 1100–1110, <https://doi.org/10.1039/d2ee03936b>.
- [9] X.P. Wang, S.B. Xi, W.S.V. Lee, P.G. Huang, P. Cui, L. Zhao, W.C. Hao, X.S. Zhao, Z. B. Wang, H.J. Wu, H. Wang, C.Z. Diao, A. Borgna, Y.H. Du, Z.G. Yu, S. Pennycook, J.M. Xue, Materializing efficient methanol oxidation via electron delocalization in nickel hydroxide nanoribbon, *Nat. Commun.* 11 (2020) 4647, <https://doi.org/10.1038/s41467-020-18459-9>.
- [10] Y.P. Wu, J.W. Tian, S. Liu, B. Li, J. Zhao, L.F. Ma, D.S. Li, Y.Q. Lan, X.H. Bu, Bi-microporous metal-organic frameworks with cubane [M<sub>4</sub>(OH)<sub>4</sub>] (M=Ni, Co) clusters and pore-space partition for electrocatalytic methanol oxidation reaction, *Angew. Chem. Int. Ed.* 58 (2019) 12185–12189, <https://doi.org/10.1002/anie.201907136>.
- [11] A.A. Dubale, Y.Y. Zheng, H.L. Wang, R. Hübner, Y. Li, J. Yang, J.W. Zhang, Navpreet Kaur Sethi, L.Q. He, Z.K. Zheng, W. Liu, High-performance bismuth-doped nickel aerogel electrocatalyst for the methanol oxidation reaction, *Angew. Chem. Int. Ed.* 59 (2020) 13891–13899, <https://doi.org/10.1002/anie.202004314>.
- [12] R. Rizo, R.M. Arán-Ais, E. Padgett, D.A. Müller, M.J. Lázaro, J. Solla-Gullón, J. M. Feliu, E. Pastor, H.D. Abruña, Pt-richcore/ Sn-richsurface/Pt<sub>skin</sub> nanocubes as highly active and stable electrocatalysts for the ethanol oxidation reaction, *J. Am. Chem. Soc.* 140 (2018) 3791–3797, <https://doi.org/10.1021/jacs.8b00588>.
- [13] A.G. Oshchepkov, G. Braesch, A. Bonnefont, E.R. Savinova, M. Chatenet, Recent advances in the understanding of nickel-based catalysts for the oxidation of hydrogen-containing fuels in alkaline media, *ACS Catal.* 10 (2020) 7043–7068, <https://doi.org/10.1021/acscatal.0c00101>.
- [14] W. Chen, C. Xie, Y.Y. Wang, Y.Q. Zou, C.L. Dong, Y.C. Huang, Z.H. Xiao, Z.X. Wei, S.Q. Du, C. Chen, B. Zhou, J.M. Ma, S.Y. Wang, Activity origins and design principles of nickel-based catalysts for nucleophile electrooxidation, *Chem* 6 (2020) 2974–2993, <https://doi.org/10.1016/j.chempr.2020.07.022>.
- [15] X. Cui, P. Xiao, J. Wang, M. Zhou, W.L. Guo, Y. Yang, Y.J. He, Z.W. Wang, Y. K. Yang, Y.H. Zhang, Z.Q. Lin, Highly branched metal alloy networks with superior activities for the methanol oxidation reaction, *Angew. Chem. Int. Ed.* 56 (2017) 4488–4493, <https://doi.org/10.1002/anie.201701149>.
- [16] Z.Y. Wang, L. Xu, F.Z. Huang, L.B. Qu, J.T. Li, K.A. Owusu, Z.A. Liu, Z.F. Lin, B. H. Xiang, X. Liu, K.N. Zhao, X.B. Liao, W. Yang, Y.B. Cheng, L.Q. Mai, Copper-nickel nitride nanosheets as efficient bifunctional catalysts for hydrazine-assisted electrolytic hydrogen production, *Adv. Energy Mater.* 9 (2019) 1900390, <https://doi.org/10.1002/aenm.201900390>.
- [17] X.J. Zhu, X.Y. Dou, J. Dai, X.D. An, Y.Q. Guo, L.D. Zhang, S. Tao, J.Y. Zhao, W. S. Chu, X.C. Zeng, C.Z. Wu, Y. Xie, Metallic nickel hydroxide nanosheets give superior electrocatalytic oxidation of urea for fuel cells, *Angew. Chem. Int. Ed.* 55 (2016) 12465–12469, <https://doi.org/10.1002/anie.201606313>.
- [18] X.L. Chen, X. Zhong, B.W. Yuan, S.Q. Li, Y.B. Gu, Q.Q. Zhang, G.L. Zhuang, X.N. Li, S.W. Deng, J.G. Wang, Defect engineering of nickel hydroxide nanosheets by Ostwald ripening for enhanced selective electrocatalytic alcohol oxidation, *Green. Chem.* 21 (2019) 578–588, <https://doi.org/10.1039/C8GC03451F>.
- [19] H. Cheng, B.H. Dong, Q. Liu, F.X. Wang, Direct electrocatalytic methanol oxidation on MoO<sub>3</sub>/Ni(OH)<sub>2</sub>: exploiting synergetic effect of adjacent Mo and Ni, *J. Am. Chem. Soc.* 145 (2023) 26858–26862, <https://doi.org/10.1021/jacs.3c09399>.
- [20] X.Y. Chia, M. Pumera, Characteristics and performance of two-dimensional materials for electrocatalysis, *Nat. Catal.* 1 (2018) 909–921, <https://doi.org/10.1038/s41929-018-0181-7>.
- [21] Y. Wang, Y.Q. Zhu, Z.H. Xie, S.M. Xu, M. Xu, Z.Z. Li, L. Ma, R.X. Ge, H. Zhou, Z. H. Li, X.G. Kong, L.R. Zheng, J.H. Zhou, H.H. Duan, Efficient electrocatalytic oxidation of glycerol via promoted OH\* generation over single-atom-bismuth-doped spinel Co<sub>3</sub>O<sub>4</sub>, *ACS Catal.* 12 (2022) 12432–12443, <https://doi.org/10.1021/acscatal.2c03162>.
- [22] W.Z. Wu, C.Y. Niu, C. Wei, Y. Jia, C. Li, Q. Xu, Activation of MoS<sub>2</sub> basal planes for hydrogen evolution by zinc, *Angew. Chem. Int. Ed.* 58 (2019) 2029–2033, <https://doi.org/10.1002/anie.201812475>.



- [23] H. Xiao, H. Shina, W.A. Goddard III, Synergy between Fe and Ni in the optimal performance of (Ni,Fe)OOH catalysts for the oxygen evolution reaction, *PNAS* 15 (2018) 5872–5877, <https://doi.org/10.1073/pnas.1722034115>.
- [24] J. Xiong, J. Di, J.X. Xia, W.S. Zhu, H.M. Li, Surface defect engineering in 2D nanomaterials for photocatalysis, *Adv. Funct. Mater.* 28 (2018) 1801983, <https://doi.org/10.1002/adfm.201801983>.
- [25] A. Zhang, Y.X. Liang, H. Zhang, Z.G. Geng, J. Zeng, Doping regulation in transition metal compounds for electrocatalysis, *Chem. Soc. Rev.* 50 (2021) 9817–9844, <https://doi.org/10.1039/D1CS00330E>.
- [26] C. Lin, Z.F. Gao, F. Zhang, J. Yang, B. Hui, J. Liu, Jin, In situ growth of single-layered  $\alpha$ -Ni(OH)<sub>2</sub> nanosheets on a carbon cloth for highly efficient electrocatalytic oxidation of urea, *J. Mater. Chem. A* 6 (2018) 13867–13873, <https://doi.org/10.1039/C8TA05064C>.
- [27] Y.X. Sun, H.Y. Shin, F.Y. Wang, B.L. Tian, C.W. Chiang, S.T. Liu, X.S. Li, Y.Q. Wang, L.Y. Tang, W.A. Goddard, M.N. Ding, Highly selective electrocatalytic oxidation of amines to nitriles assisted by water oxidation on metal-doped  $\alpha$ -Ni(OH)<sub>2</sub>, *J. Am. Chem. Soc.* 144 (2022) 15185–15192, <https://doi.org/10.1021/jacs.2c05403>.
- [28] W.L. Yang, X.D. Zhang, Y. Xie, Advances and challenges in chemistry of two-dimensional nanosheets, *Nano Today* 11 (2016) 793–816, <https://doi.org/10.1016/j.nantod.2016.10.004>.
- [29] Y.F. Sun, S. Gao, F.C. Lei, C. Xiao, Y. Xie, Ultrathin two-dimensional inorganic materials: new opportunities for solid state nanochemistry, *Acc. Chem. Res.* 48 (2014) 3–12, <https://doi.org/10.1021/ar500164g>.
- [30] A.G. Krasnov, M.S. Koroleva, M.I. Vlasov, I.R. Shein, I.V. Piir, D.G. Kellerman, Ab initio and experimental insights on structural, electronic, optical, and magnetic properties of Cr-doped Bi<sub>2</sub>Ti<sub>2</sub>O<sub>7</sub>, *Inorg. Chem.* 58 (2019) 9904–9915, <https://doi.org/10.1021/acs.inorgchem.9b01057>.
- [31] X.Q. Sun, Y.H. Xie, F.F. Wu, H.M. Chen, M.L. Lv, S. Ni, G. Liu, X.X. Xu, Photocatalytic hydrogen production over chromium doped layered perovskite Sr<sub>2</sub>TiO<sub>4</sub>, *Inorg. Chem.* 54 (2015) 7445–7453, <https://doi.org/10.1021/acs.inorgchem.5b01042>.
- [32] Z.Y. Chen, Y. Song, J.Y. Cai, X.S. Zheng, D.D. Han, Y.S. Wu, Y.P. Zang, S.W. Niu, Y. Liu, J.F. Zhu, X.J. Liu, G.M. Wang, Tailoring the d-band centers enables Co<sub>4</sub>N nanosheets to be highly active for hydrogen evolution catalysis, *Angew. Chem. Int. Ed.* 57 (2018) 5076–5080, <https://doi.org/10.1002/anie.201801834>.
- [33] M.W. Gu, H.H. Peng, I.W.P. Chen, C.H. Chen, Tuning surface d bands with bimetallic electrodes to facilitate electron transport across molecular junctions, *Nat. Mater.* 20 (2021) 658–664, <https://doi.org/10.1038/s41563-020-00876-2>.
- [34] S.L. Li, R.G. Ma, J.C. Hu, Z.C. Li, L.J. Liu, X.L. Wang, Y. Lu, G.E. Sterbinsky, S. H. Liu, L. Zheng, J. Liu, D.M. Liu, J.C. Wang, Coordination environment tuning of nickel sites by oxyanions to optimize methanol electro-oxidation activity, *Nat. Commun.* 13 (2022) 2916, <https://doi.org/10.1038/s41467-022-30670-4>.
- [35] C.H. Huang, X.X. Song, Y.L. Qin, B.H. Xu, H.C. Chen, Cation exchange reaction derived amorphous bimetal hydroxides as advanced battery materials for hybrid supercapacitors, *J. Mater. Chem. A* 6 (2018) 21047–21055, <https://doi.org/10.1039/C8TA07609J>.
- [36] C. Srilakshmi, R. Saraf, V. Prashanth, G.M. Rao, C. Shivakumara, Structure and catalytic activity of Cr-doped BaTiO<sub>3</sub> nanocatalysts synthesized by conventional oxalate and microwave assisted hydrothermal methods, *Inorg. Chem.* 55 (2016) 4795–4805, <https://doi.org/10.1021/acs.inorgchem.6b00240>.
- [37] V. Martis, R. Oldman, R. Anderson, M. Fowles, T. Hyde, R. Smith, S. Nikitenko, W. Bras, G. Sankar, Structure and speciation of chromium ions in chromium doped Fe<sub>2</sub>O<sub>3</sub> catalysts, *Phys. Chem. Chem. Phys.* 15 (2013) 168–175, <https://doi.org/10.1039/C2CP43307A>.
- [38] H.B. Li, M.H. Yu, F.X. Wang, P. Liu, Y. Liang, J. Xiao, C.X. Wang, Y.X. Tong, G. W. Yang, Amorphous nickel hydroxide nanospheres with ultrahigh capacitance and energy density as electrochemical pseudocapacitor materials, *Nat. Commun.* 4 (2013) 1894, <https://doi.org/10.1038/ncomms2932>.
- [39] J.S. Sun, Y.T. Zhou, R.Q. Yao, H. Shi, Z. Wen, X.Y. Lang, Q. Jiang, Nanoporous gold supported chromium-doped NiFe oxyhydroxides as high-performance catalysts for the oxygen evolution reaction, *J. Mater. Chem. A* 7 (2019) 9690–9697, <https://doi.org/10.1039/C9TA01027K>.
- [40] O. Dvornenko, S.-L. Lo, Y.-J. Chen, G.W. Chen, H.-M. Tsai, Y.-L. Wang, J.-K. Wang, Speciation analysis of Cr(VI) and Cr(III) in water with surface-enhanced raman spectroscopy, *ACS Omega* 6 (2021) 2052–2059, <https://doi.org/10.1021/acsomega.0c05020>.
- [41] M.L. Yuan, S.B. Dipazir, M. Wang, Y. Sun, D.L. Gao, Y.L. Bai, M. Zhang, P.L. Lu, H. Y. He, X.Y. Zhu, S.W. Bai, Z.J. Liu, Z.P. Luo, G.J. Zhang, Polyoxometalate-assisted formation of CoSe/MoSe<sub>2</sub> heterostructures with enhanced oxygen evolution activity, *J. Mater. Chem. A* 7 (2019) 3317–3326, <https://doi.org/10.1039/C8TA11976G>.
- [42] Y. Wang, X.P. Li, M.M. Zhang, Y.G. Zhou, D.W. Rao, C. Zhong, J.F. Zhang, X. P. Han, W.B. Hu, Y.C. Zhang, K. Zaghbi, Y.S. Wang, Y.D. Deng, Lattice-strain engineering of homogeneous NiSe<sub>0.5</sub>Se<sub>0.5</sub> core-shell nanostructure as a highly efficient and robust electrocatalyst for overall water splitting, *Adv. Mater.* 32 (2020) 2000231, <https://doi.org/10.1002/adma.202000231>.
- [43] G.F. Hu, L. Shang, T. Sheng, Y.G. Chen, L.Y. Wang, PtCo@NCs with short heteroatom active site distance for enhanced catalytic properties, *Adv. Funct. Mater.* 30 (2020) 2002281, <https://doi.org/10.1002/adfm.202002281>.
- [44] L.F. Fan, Y.X. Ji, G.X. Wang, J.X. Chen, K. Chen, X. Liu, Z.H. Wen, High entropy alloy electrocatalytic electrode toward alkaline glycerol valorization coupling with acidic hydrogen production, *J. Am. Chem. Soc.* 144 (2022) 7224–7235, <https://doi.org/10.1021/jacs.1c13740>.
- [45] J.S. Li, R.L. Wei, X. Wang, Y. Zuo, X. Han, J. Arbiol, J. Llorca, Y.Y. Yang, A. Cabot, C.H. Cui, Selective methanol-to-formate electrocatalytic conversion on branched nickel carbide, *Angew. Chem. Int. Ed.* 59 (2020) 20826–20830, <https://doi.org/10.1002/anie.202004301>.
- [46] Y.X. Chen, Atsushi Miki, S. Ye, H. Sakai, M. Osawa, Formate, an active intermediate for direct oxidation of methanol on Pt electrode, *J. Am. Chem. Soc.* 125 (2003) 3680–3681, <https://doi.org/10.1021/ja029044t>.